Korean J. Chem. Eng., 38(7), 1522-1528 (2021)
DOI: 10.1007/s11814-021-0800-x

pISSN: 0256-1115
eISSN: 1975-7220

Influence of post-heat treatment on photocatalytic activity in metal-embedded TiO_2 nanofibers

Hyo-Young Kim* and Young-Wan Ju*,,†**

*Department of Chemical Engineering, College of Engineering, Wonkwang University, Iksan, Jeonbuk 54538, Korea
**Nanoscale Sciences and Technology Institute, Wonkwang University, Iksan, Jeonbuk 54538, Korea
(*Received 18 January 2021 • Revised 22 March 2021 • Accepted 4 April 2021*)

Abstract−With the increasing concerns for environmental pollution, photocatalysts have been attracting attention due to their environmentally friendly characteristics, low cost, and simple processing. Titanium dioxide (TiO_2) has been commonly used as a photocatalyst owing to its white pigment, excellent photocatalytic activity and low cost; however, its poor pollutant adsorption properties and high electron-hole recombination ratio limit its practical application. Transition metals such as nickel exhibit excellent electron-trapping capability, lowering the rate of electron-hole recombination and facilitating the generation of oxygen free radicals. One-dimensional nanofibers fabricated by electrospinning methods not only develop mesopores but can also make photocatalytic materials with a relatively high specific surface area, thereby increasing the adsorption of pollutants. In this study, transition metal-embedded TiO_2 was fabricated by an electrospinning method, and the influence of post-calcination in a reducing atmosphere on the photocatalytic activity was investigated. The photocatalytic properties were performed by decomposition of Rhodamine B under visible light irradiation using fabricated material. Among the investigated samples, Ni-embedded TiO_2 nanofibers showed the fastest decomposition of Rhodamine B under visible light irradiation due to a relatively high number of oxygen vacancies, lower Fermi level, small particle size, well-developed mesopores and relatively high specific surface area.

Keywords: Photocatalytic Activity, Nanofiber, Electrospinning, Exsolution, Rhodamine B Degradation

INTROUDCTION

In recent years, rapid developments in science technology and industry have resulted in increasing of the environmental pollution problems. To protect the environment, methods for the decomposition of problematic environmental pollutants have attracted attention [1]. Existing method of pollutant decomposition uses organic compounds. However, the method is limited due to the toxicity, high cost, and low processing efficiency associated with organic compounds [2]. As an environmentally friendly method, decomposing pollutants using photocatalysis has been considered a promising alternative, as it can be conducted using only solar energy at room temperature [3]. Therefore, the environment protection is achieved through photocatalysts with high activity.

Titanium dioxide (TiO_2) is a promising photocatalyst material [4] and it is a widely used owing to its excellent chemical stability over a wide pH range, low toxicity, low cost, high durability, and environmentally friendly properties [5,6]. Nevertheless, the photocatalytic efficiency of TiO_2 is limited due to its electron-hole recombination ratio and wide bandgap energy (3.2 eV), suggesting it is only activated in the ultraviolet region [7-9]. As the ultraviolet region comprises only 5% of sunlight [10], research has been conducted for activation in the visible light region that comprises a higher proportion (45%) than ultraviolet light [11]. The efficient utilization of sunlight is considered as an important factor in photocatalysis [4]. To overcome this issue, previous studies attempted to improve the photocatalytic activity of TiO_2 using transition metals to activate the visible light region [4]. Doping the transition metal separates electrons and holes on the surface of TiO_2 photocatalysts and inhibits electron-hole recombination [12]. Furthermore, catalytic activity increases and the absorbance of photocatalyst is shifted to the visible light region [13-18]. Pt, Au, Pd, Ni, and Ag, which are used as doping materials to increase photocatalytic activity, have lower Fermi levels than TiO_2 [16,17]. Electrons generated by sunlight are transferred from the conduction band to the metal, and holes remain in the valence band [18]. Among these dopant materials, Ni is easily doped on the TiO_2 lattice, and the Ni dopant affects the TiO_2 band gap reduction. Guan et al. [19] reported reducing of the band gap in photocatalysts was achieved by doping nickel. As the incorporation of Ni ions into TiO_2 lattice, the band gap of TiO_2 reduces due to the formation of impurity levels below conduction band, and electrons can transfer from valence band. These electrons adsorbed by O_2 in surface and produce $\bullet O_2$ ions that can further convert to the strong redox species •OH ions. Nagaraj et al. [20] reported Ni^{2+} can easily be doped into TiO_2 lattice by substitution of Ti^{4+} and generate an impurity energy level. This impurity energy induces to strong visible light response of photocatalyst, resulting in the increased photocatalytic activity.

To increase the photocatalytic efficiency, the adsorption of pollutants on photocatalysts should be improved [14]. The pollutant adsorption property of a photocatalyst can vary depending on the pore size [15]. The development of mesopores enables the adsorption of large amounts of pollutants and increases the photocatalytic efficiency [21,22]. Electrospinning is a unique and simple method

†To whom correspondence should be addressed.
E-mail: ywju1978@wku.ac.kr

for fabricating nanofiber-type materials with large surface areas and well-developed mesopores [23,24]. This method can produce a one-dimensional fiber material from a liquid solution using an electric field generated at high voltage [25-27]. The electrospinning method involves the fabrication of nanofibers from a mixed solution of organic polymers and inorganic materials [18]. The resultant material is bestowed with the characteristics of inorganic materials with high strength, high heat resistance, thermal stability, chemical resistance, and the variable characteristics of organic materials [28]. The fabrication of organic-inorganic composite materials via the electrospinning involves calcination at high temperature and the organic polymer is decomposed to obtain inorganic nanofibers.

In this study, TiO_2 and Ni-doped TiO_2 nanofibers were fabricated using an electrospinning method. Then, they were subjected to a simple calcination process in a reducing atmosphere to prepare Black-TiO_2 and Ni-exsoluted TiO_2 nanofibers. In addition, the influence of oxygen vacancies on the photocatalytic activity of the prepared nanofiber samples was investigated by studying the decomposition reaction of Rhodamine B under visible light irradiation.

MATERIALS AND METHODS

TiO_2 nanofibers were fabricated by electrospinning a polymer solution consisting of the desired titanium precursor and Poly (vinyl acetate) (PVAc, $[CH_2CH(O_2CCH_3)]_n$, Mw~500,000, Sigma-Aldrich Co., Inc.) dissolved in N, N-dimethylformamide (DMF, $(CH_3)_2NCOH$, 99.0%, Samchun Pure Chemical Co., Ltd.). First, 11 wt% PVAc polymer solution was stirred at 353 K. After the polymer was completely dissolved in DMF, 0.3 mL acetic acid (CH_3COOH; $C_2H_4O_2$, 99.7%, Daejung Chemicals & Metals Co., Ltd.) was added and stirred at room temperature for 10 min. Then, 0.005 mol of titanium(IV) butoxide ($Ti(OCH_2CH_2CH_2CH_3)_4$, 97%, Sigma-Aldrich Co., Inc.) was added to the prepared PVAc polymer solution. The PVAc polymer solution containing titanium precursors was stirred at 373 K for 1 h. The composite solution was electrospun in the form of a fiber web through a positively charged capillary tip of 0.5 mm diameter using a high-voltage power supply (HV30, NanoNC Co., Ltd.). The electrospun fibers were collected as a web on a drum-type metal collector (NNC-DC90H, Ø90, NanoNC Co., Ltd.) rotating at approximately 290 rpm. For electrospinning, the supplied voltage was 20 kV, distance from the collector to the syringe needle tip was 13 cm, and flow velocity of the solution was adjusted to 0.8 mL/h using a syringe pump. Electrospun fibers were calcined to decompose the PVAc polymer at 773 K for 2 h. Black-TiO_2 nanofibers were fabricated by calcining the TiO_2 nanofibers at 923 K for 4 h in a hydrogen atmosphere.

Ni-doped TiO_2 nanofibers were fabricated by adding a nickel precursor to the PVAc polymer solution to which the titanium precursor was added. Nickel(II) acetate tetrahydrate ($Ni(OCOCH_3)_2 \cdot 4H_2O$, 98%, Sigma-Aldrich Co., Inc.) was added in a quantity corresponding to 2 wt% of the titanium precursor contained in the PVAc polymer solution. The PVAc polymer solution containing titanium and nickel precursors was stirred at 373 K for 1 h. The composite solution was electrospun in the form of a fiber web using the same electrospinning conditions stated above. Electrospun fibers were calcined to decompose the PVAc polymer at 773 K for 2 h to yield Ni-doped TiO_2 nanofibers. Ni-exsoluted TiO_2 nanofibers were fabricated by calcining the Ni-doped TiO_2 nanofibers at 923 K for 4 h in a hydrogen atmosphere using high purity hydrogen gas (99.99%).

The fabricated TiO_2, Black-TiO_2, Ni-doped TiO_2, and Ni-eluted TiO_2 nanofibers were named TiO_2, B-TiO_2, ND-TiO_2 and NE-TiO_2, respectively.

Morphological observations and quantitative elemental analysis of the TiO_2, B-TiO_2, ND-TiO_2 and NE-TiO_2 nanofibers were conducted using scanning electron microscopy (FE-SEM, Hitachi, S-4800, Japan) and energy dispersive spectrometer (EDS, HORIBA, S-4800). Structural characterization of the fabricated nanofibers was via X-ray diffraction (XRD) using a MiniFlex 600 (Rigaku, Japan) with Cu K_α radiation (λ=1.5406 Å) in the 2θ range of 20° to 80° at 4°/min. The specific surface areas and pore size distributions were evaluated using the Brunauer Emmett Teller (BET) equation from isotherms recorded at 77 K (BELSORP-mini II, Mictrotrac BEL, USA). The oxidation state of the prepared nanofibers was determined by X-ray photoelectron spectroscopy (XPS, Thermo ESCALAB 250, USA), using Al K_α radiation. UV-VIS spectra of the samples were recorded using a Lambda365 (PerkinElmer Inc., USA) in the wavelength range of 400-700 nm. Photoluminescence spectra were obtained using a LabRAM HR-800 UV-Visible-NIR (HORIBA Jobin Yvon Inc., USA) with a 325 nm laser in a range of 340-800 nm.

The photocatalytic activity of the prepared nanofibers was determined by measuring the degradation of Rhodamine B in water. An internal 300 W Xenon lamp (DYX500, DY-Tech, Korea) was used as a UV light source, and it was equipped with an optical filter for visible light (λ>420 nm). To cool the lamps, a circulating water system was used. The initial concentration of the 100 mL Rhodamine B solution was 25 mg/L. A solid catalyst (0.05 g) was added and the solution was stirred without UV-Vis light for 2 h to obtain a good dispersion, establishing an adsorption-desorption balance between the catalyst surface and the organic molecules of Rhodamine B. After irradiation with visible light for 4 h, 4 mL of reaction solution was extracted and centrifuged at 4,000 rpm for 10 min. Then, the filtrates were analyzed by using UV-VIS spectrophotometer to calculate the decrease in Rhodamine B concentration.

RESULTS AND DISCUSSION

Fig. 1 shows the morphology of the fabricated fiber samples. The as-prepared composite fibers, as shown in Fig. 1(a) and (d), were partially aligned along the winding direction of the drum winder. The surfaces of the fibers were smooth and uniform owing to the amorphous nature of PVAc, and the average diameter of both fibers was 138 nm. This indicates that the Ni additive did not significantly affect solution parameters such as viscosity and electric conductivity in electrospinning. TiO_2 and ND-TiO_2 nanofibers were obtained through calcination of Ti-embedded PVAc fibers and Ti, Ni-embedded PVAc fibers, respectively. As shown in Fig. 1(b) and (e), the surfaces of the TiO_2 and ND-TiO_2 nanofibers shrank and increased in roughness due to the decomposition of PVAc during the calcination process [29]. In both samples, the diameter of the

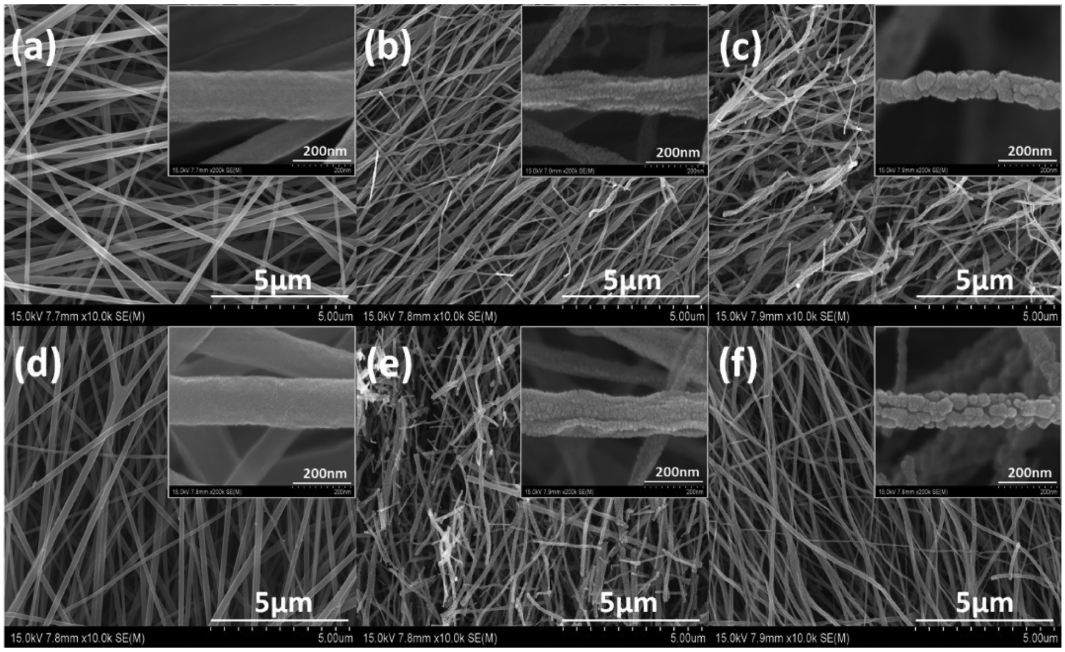

Fig. 1. FE-SEM image of (a) as-spun Ti-embedded PVAc fiber, (b) Ti-embedded fibers calcined at 773 K, (c) Ti-embedded fibers calcined at 923 K in H_2, (d) as-spun Ti, Ni-embedded PVAc fiber (e) Ti, Ni-embedded fibers calcined at 773 K and (f) Ti, Ni-embedded fibers calcined at 923 K in H_2.

fiber was decreased by decomposition of the PVAc polymer during the calcination process. The average diameters of the TiO_2 and ND-TiO_2 nanofibers were 107 nm and 121 nm, respectively. ND-TiO_2 exhibited a thicker average fiber diameter as a result of the increase in grain size caused by the Ni doping and grain agglomeration. The influence of transition metal dopants in semiconductor materials has been investigated by many research groups [30-32]. Manzoor et al. reported that the position of the ion in the lattice can be determined from the ionic size difference between the host and dopant [31]. Because the ionic radius of Ni^{2+} (69 pm) is larger than that of Ti^{4+} (61 pm), Ni^{2+} ions can substitute into Ti^{4+} sites by an interstation process, which could produce a positive charge around the Ti^{4+} host ion or create oxygen vacancies. Therefore, the diameter of the nanofiber and the grain size increased upon doping with Ni. B-TiO_2 and NE-TiO_2 nanofibers were fabricated by additional heat treatment of TiO_2 and ND-TiO_2 nanofibers at 923 K in a hydrogen atmosphere. After post-heat treatment, dark gray nanofibers were obtained. The particles constituting the nanofibers were densified due to crystallization of titanium dioxide on the surface [33]. In addition, the surface roughness of the nanofibers increased and the diameters of nanofibers shrank, as shown in Fig. 1(c) and (f). The average diameters of the B-TiO_2 and NE-TiO_2 nanofibers were 77 nm and 92 nm, respectively. These changes originate from the vigorous sintering at relatively high temperatures.

To confirm the influence of the Ni dopant and post-heat treatment, X-ray diffraction (XRD) analysis was conducted. Fig. 2(a) shows the XRD patterns of anatase phase TiO_2 nanofibers were fabricated without any impurities. In addition, the ND-TiO_2 exhibited only the typical XRD patterns of anatase phase TiO_2 without any secondary phase, that including Ni-related peaks as shown in

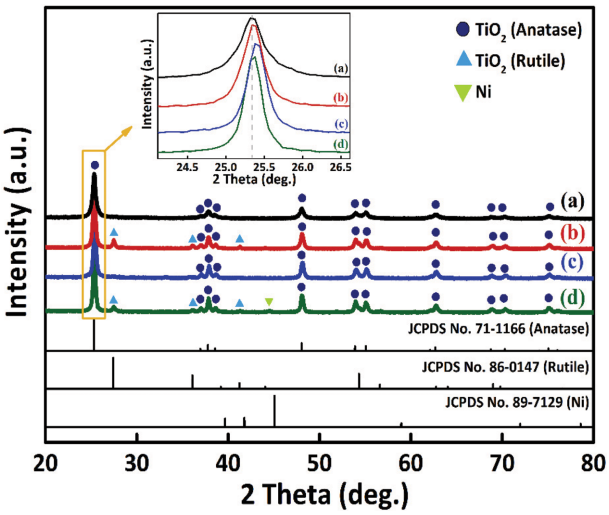

Fig. 2. X-ray diffraction (XRD) patterns of (a) TiO_2, (b) B-TiO_2, (c) ND-TiO_2 and (d) NE-TiO_2.

Fig. 2(c). This indicates that the Ni dopant was successfully incorporated into TiO_2, and it did not contribute to the formation of any secondary phases that included the rutile or brookite phases TiO_2. The Ni dopant did not cause formation of secondary phase materials; however, it did result in peaks shifting to a higher 2θ angle than in the XRD patterns of TiO_2, because the radius of the nickel ion (0.69 Å) is larger than that of titanium ion (0.61 Å) [13]. As mentioned, when doped with a material of smaller ionic radius, oxygen vacancies can be formed. Fig. 2(b) and (d) show the XRD patterns of B-TiO_2 and NE-TiO_2 prepared by post-heat treatment in a reducing atmosphere of TiO_2 and ND-TiO_2, respectively. The

XRD patterns of B-TiO_2 and NE-TiO_2 show the diffraction peaks of anatase and rutile phase TiO_2. The rutile phase is active under visible light but exhibits a lower bandgap (3.0 eV) compared to that of anatase phase. This results in low photocatalytic activity due to a high ratio of electron-hole recombination [34]. Therefore, the fabricated B-TiO_2 and NE-TiO_2 nanofibers with rutile peaks can affect to decrease photocatalytic activity. In addition, compared with the TiO_2 and ND-TiO_2 nanofibers, the crystallinity of the B-TiO_2 and NE-TiO_2 nanofibers increased according to the post-heat treatment at higher temperatures. The crystallite sizes of TiO_2, ND-TiO_2, B-TiO_2 and NE-TiO_2 nanofibers calculated by the Scherrer equation were 21.76 nm, 27.99 nm, 26.34 nm and 30.83 nm, respectively. The post-heat treatment in a reducing atmosphere affected not only the crystallite size but also the lattice structure [33]. The XRD pattern of B-TiO_2 exhibited peak shift to higher 2θ angles than that of TiO_2. These peak shifts are related to the change in the oxidation state of titanium from Ti^{4+} (0.61 Å) to Ti^{3+} ions (0.67 Å), which can affect the formation of oxygen vacancies. In contrast, NE-TiO_2 prepared through the same post-treatment process exhibited peak shift toward a lower 2θ angle compared to ND-TiO_2. The difference in peak shift trends may be related to the Ni diffraction peaks, which indicate the exsolution of Ni dopant during post-heat treatment in a reducing atmosphere. Exsolution has previously used to produce "intelligent catalyst" in the field of automotive catalysis [32]. Nishihata et al. reported the exsolution of noble metals from a noble metal-doped perovskite lattice during sintering in a reducing atmosphere. The exsolution process has been widely applied in various catalyst area because the exsolved nanoparticles are stuck

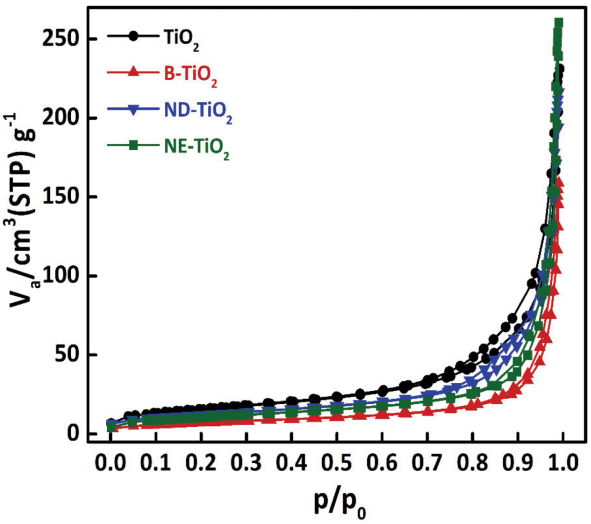

Fig. 3. Nitrogen adsorption-desorption isotherms of TiO_2, B-TiO_2, ND-TiO_2 and NE-TiO_2.

on the surface without agglomeration during the redox cycle. During post-heat treatment in a reducing atmosphere, NE-TiO_2 was formed by the Ni^{2+} ions that were exsolved from the ND-TiO_2 lattice and rutile phase TiO_2 was formed. Additionally, SEM-EDS analysis was conducted to confirm exsolution of Ni. The content of the Ni element increased from 0.85 wt% (ND-TiO_2) to 1.94 wt% (NE-TiO_2) after the post-heat treatment process. Deka et al. reported increasing content of metal elements after the post-heat treatment pro-

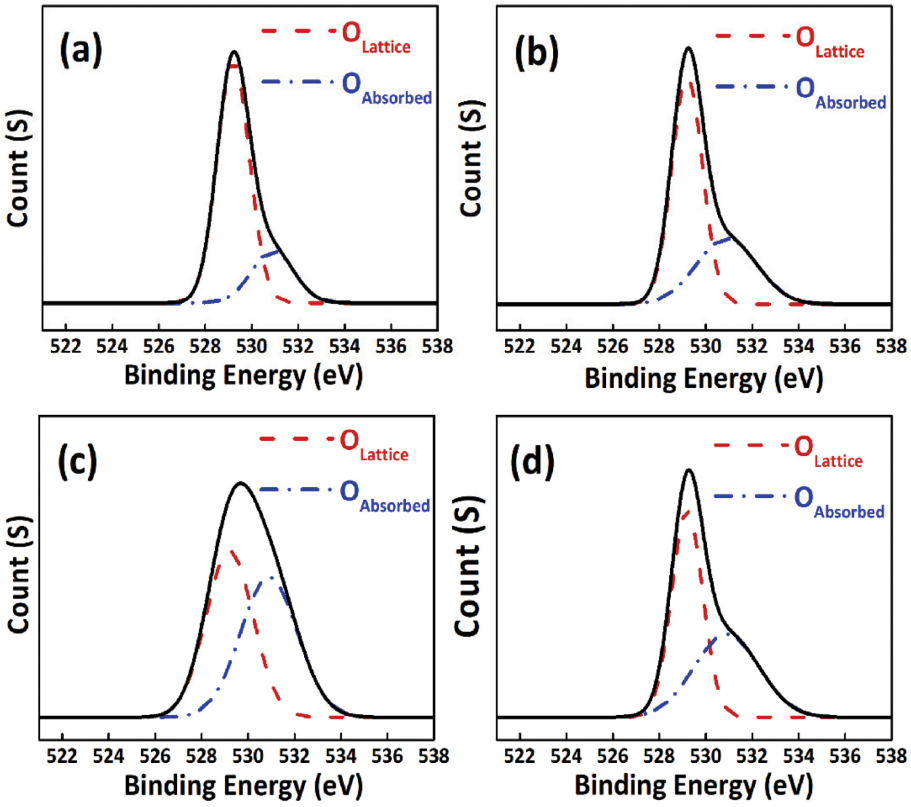

Fig. 4. O 1s X-ray photoelectron spectroscopy (XPS) spectra (a) TiO_2, (b) B-TiO_2, (c) ND-TiO_2 and (d) NE-TiO_2.

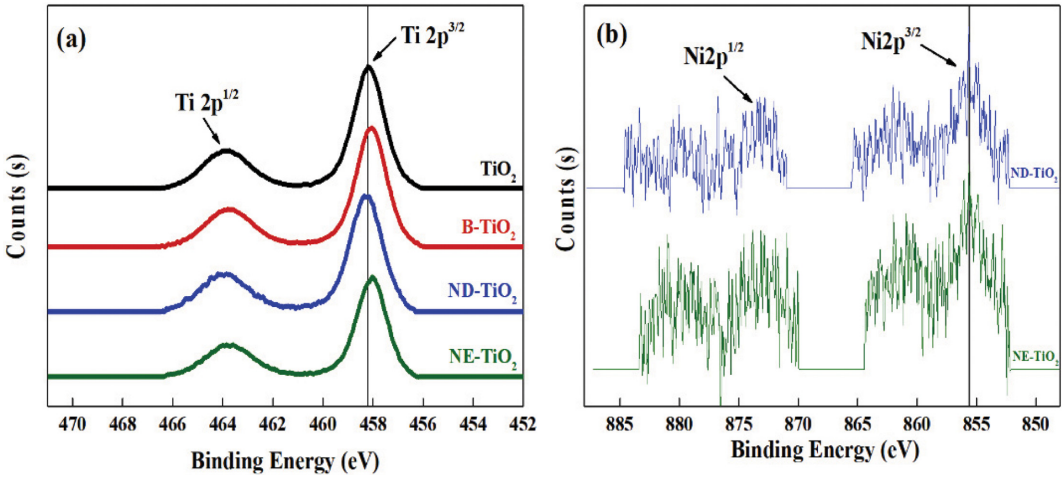

Fig. 5. (a) Ti 2p and (b) Ni 2p X-ray photoelectron spectroscopy (XPS) spectra of sample.

cess in EDS analysis indicates the exsolution of metal [35].

For photocatalyst, the specific surface area is an important factor in determining the adsorption of pollutants such as Rhodamine B and the photochemical reaction area. Fig. 3 shows the nitrogen adsorption-desorption isotherms of TiO_2, B-TiO_2, ND-TiO_2 and NE-TiO_2. The specific surface areas were calculated using the Brunauer Emmett Teller (BET) equation of TiO_2, B-TiO_2, ND-TiO_2 and NE-TiO_2 nanofibers were 55.56 m^2/g, 26.63 m^2/g, 43.09 m^2/g and 38.57 m^2/g, respectively. The TiO_2 and ND-TiO_2 nanofibers had high specific surface area compared to the nanofibers that conducted post-heat treatment at 923 K. Through the post-heat treatment process the diameter of the fiber decreased, and the specific surface area decreased because the particle size increased and structure densified [36]. All samples can be described as typical IUPAC type III, which indicates nonporous or macroporous materials. A hysteresis loop was observed in the high relative pressure range from 0.7 to 1.0 of the isotherms of TiO_2 and ND-TiO_2, which indicates the development of a mesoporous type in the samples. After post-heat treatment, ND-TiO_2 showed a small decrease in the specific surface area, which may be related to the exsolution of Ni particles from the ND-TiO_2 lattice as confirmed by XRD analysis.

Oxygen vacancy can affect photocatalytic activity by capturing electron in the conductive band and preventing electron-hole recombination. The oxygen vacancy ratios of the fabricated nanofiber samples was calculated from the O1s X-ray photoelectron spectra, as shown in Fig. 4. The integral value of absorbed oxygen (O_{Ab}) to lattice oxygen (O_L) in each of the fabricated nanofibers was calculated. B-TiO_2 nanofibers (O_{Ab}/O_L=0.5) increase the formation of oxygen vacancies compared to TiO_2 nanofibers (O_{Ab}/O_L=0.28). The oxidation state of titanium was reduced from Ti^{4+} to Ti^{3+} during heat treatment in a hydrogen atmosphere for fabricating B-TiO_2 from TiO_2. In this process, oxygen vacancies were formed in order to achieve electrical neutrality. ND-TiO_2 nanofibers (O_{Ab}/O_L=1.0) had the highest number of oxygen vacancies due to the oxidation state of Ni^{2+} ions. In Ni-doped TiO_2, Ni^{2+} occupied Ti^{4+} sites and oxygen vacancies were formed due to the lower oxidation state. In the NE-TiO_2 nanofibers (O_{Ab}/O_L=0.8), the oxidation state of titanium was converted from Ti^{4+} to Ti^{3+} through post-heat treatment in a reducing atmosphere and formed oxygen vacancies [37]. However, the exsolution of Ni decreased the formation of oxygen vacancies compared to the ND-TiO_2 nanofibers. After post-heat treatment in a reducing atmosphere, Ni exsoluted on the ND-TiO_2 nanofibers surface and the ratio of Ni^{2+} ions occupying the titanium sites was decreased. The formation of many oxygen vacancies inhibits electron-hole recombination by trapping electrons that are formed upon irradiating with light [38,39]. Therefore, the ND-TiO_2 nanofibers with the highest oxygen vacancies formation affected to improve photocatalytic activity.

Fig. 5 displays the XPS spectra for the Ti 2p and Ni 2P of nanofibers after heat treatment in hydrogen atmosphere. Fig. 5(a) shows the Ti 2p XPS spectra of as-prepared pure TiO_2 and B-TiO_2, ND-TiO_2 and NE-TiO_2 photocatalysts. Two major peaks at 458.2 eV ($Ti\ 2p^{3/2}$) and 463.8 eV ($Ti\ 2p^{1/2}$) are observable for pure TiO_2, These values are characteristic of octahedral Ti^{4+} in TiO_2. In contrast, heat treatment nanofibers at 923 K show a shift in the spectrum. The variation of binding energy results in the shift of the corresponding XPS peak due to the presence of the chemical states of the element having different oxidation state. The appearance of shifting peak to low binding energy suggests the existence of Ti oxidation states lower than Ti^{4+} [40-42]. The creation of Ti^{3+} species could be a result of the reduction by heat treatment in hydrogen atmosphere. Fig. 5(b) shows the Ni 2p XPS spectra of as-prepared ND-TiO_2 and NE-TiO_2 photocatalysts. Two major peaks at 855.6 eV ($Ni\ 2p^{3/2}$) and 873.1 eV ($Ni\ 2p^{1/2}$) are observable for ND-TiO_2. The shifting of Ni XPS spectra to low binding energy indicates that the Ni oxidation state is lower that Ni^{2+}. Because, Ni^{2+} ions occupying the titanium sites in ND-TiO_2 are exsoluted and reduction of Ni^{2+} ions after heat treatment.

The electron-hole recombination behavior of the fabricated nanofibers was investigated by photoluminescence (PL) spectroscopy. Fig. 6 shows the PL spectra of TiO_2, B-TiO_2, ND-TiO_2 and NE-TiO_2. During the PL spectroscopy, electrons in the conduction band and holes in the valence band are recombined, energy and light are released [43]. A higher ratio of recombination between electrons and holes results in a higher intensity of the peak in the PL spectrum. TiO_2 nanofibers with the lowest formation of oxygen vacan-

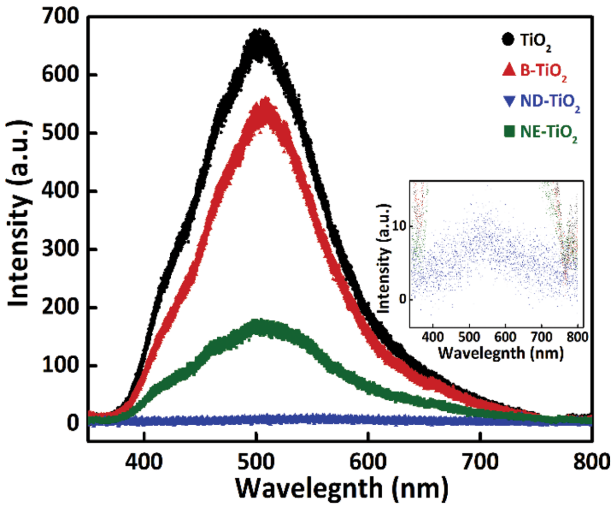

Fig. 6. Photoluminescence (PL) spectra of TiO_2, B-TiO_2, ND-TiO_2 and NE-TiO_2.

cies have poor ability to trap electrons in the conduction band. Electrons recombine with holes in the valence band due to the low number of oxygen vacancies. Therefore, the PL intensity of the TiO_2 nanofibers (650 a.u.) was higher than that of the samples. Compared with TiO_2 nanofibers, the B-TiO_2 nanofibers have a higher number of oxygen vacancies formed, and oxygen vacancies can capture more electrons, so the PL intensity of B-TiO_2 (529 a.u.) was relatively low. The rutile phase peaks that appeared in the NE-TiO_2 and B-TiO_2 nanofibers indicated an increased the ratio of electron-hole recombination and reduced photocatalytic activity. Compared with the ND-TiO_2 nanofiber, NE-TiO_2 nanofibers had an increased ratio of electron-hole recombination due to the fewer oxygen vacancies and the existence of the rutile phase. The PL intensity of NE-TiO_2 (167 a.u.) was higher than that of ND-TiO_2 (10 a.u.). ND-TiO_2 nanofibers had the lowest PL peak intensity due to the low ratio of electron-hole recombination by forming the highest number of oxygen vacancies compared to other samples.

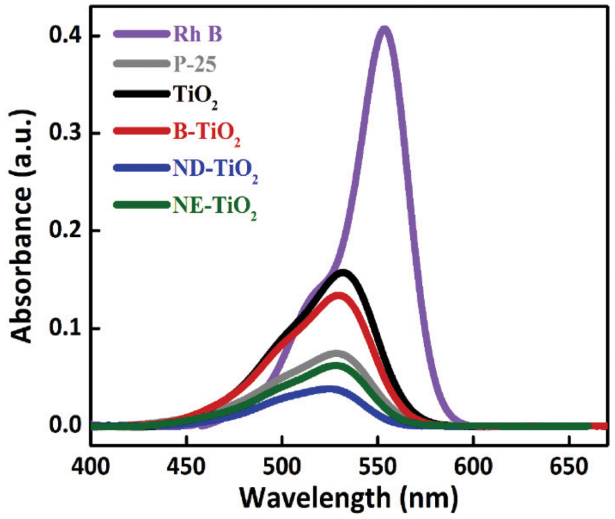

Fig. 7. UV-VIS absorption spectra of TiO_2, B-TiO_2, ND-TiO_2, NE-TiO_2 and commercial P-25 photocatalyst.

The photocatalytic property of the fabricated nanofibers was evaluated by decomposing Rhodamine B under visible light irradiation, as shown in Fig. 7. Before irradiation with visible light to evaluate the photocatalytic activity, all samples were kept in a dark room for 2 h to equilibrate the adsorption and desorption of Rhodamine B on the nanofiber surface. The concentration of Rhodamine B solution before the photolysis reaction was 0.4 arbitrary units (a.u.). As a result of decomposing Rhodamine B under visible light irradiation for 4 h, TiO_2 (0.15 a.u.) and B-TiO_2 (0.13 a.u.) had a high absorption peak intensity, indicating the slow decomposition of Rhodamine B. In contrast, after decomposing Rhodamine B under visible light irradiation for 4 h, ND-TiO_2 showed the lowest peak intensity at 0.03 a.u., which indicates the fastest decomposition rate compared to other samples. The ND-TiO_2 exhibited a decreased ratio of electron-hole recombination, which originated from a large number of oxygen vacancies and a high specific surface area with well-developed mesopores. In comparison with ND-TiO_2, NE-TiO_2 nanofibers showed relatively high absorbance peak intensity (0.06 a.u.). This may originate from the relatively high ratio of electron-hole recombination with a lower oxygen vacancy ratio, which is related to the exsolution of Ni and the formation of the rutile phase during the post-heat treatment in reducing atmosphere. Based on these results, it can be confirmed that the activity of the photocatalyst is determined by the electron-hole recombination ratio due to oxygen vacancy rather than the specific surface area. In addition, the doping of a heterogeneous element having a lower oxidation state than the reduction treatment is effective in the formation of oxygen vacancies.

CONCLUSION

TiO_2 nanofibers and 2 mol% Ni-doped TiO_2 nanofibers were fabricated by electrospinning and simple calcination process. Ni doping caused a decrease in the specific surface area as a result of the increase in grain size also enhancing the number of oxygen vacancies in the TiO_2 lattice. Black TiO_2 nanofibers and Ni-exsolved TiO_2 nanofibers were prepared from TiO_2 and Ni-doped TiO_2 nanofibers by post-heat treatment in a reducing atmosphere. In the case of the TiO_2 nanofiber, the post-heat treatment caused the formation of oxygen vacancies by reducing the oxidation state of titanium from Ti^{4+} to Ti^{3+}. In contrast, Ni-exsolved TiO_2 exhibited a reduction in the oxygen vacancy ratio in comparison with Ni-doped TiO_2 due to the Ni exsolution during post-heat treatment. The post-heat treatment caused a decrease in the diameter of the fiber, and the specific surface area was decreased because of the increased in the particle density. The influence of specific surface area and oxygen vacancy on the photocatalytic activity of the fabricated nanofibers was confirmed by studying the decomposition of Rhodamine B conducted for 4 h under visible light irradiation. The photocatalytic activity test confirmed that the activity of the photocatalyst is determined by the hole-electron recombination ratio due to oxygen vacancies rather than the specific surface area. In addition, the doping of a heterogeneous element having a lower oxidation state than the reduction treatment is effective in the formation of oxygen vacancies.

ACKNOWLEDGEMENTS

This research was supported by Wonkwang University in 2019.

REFERENCES

1. W. Ouyang, S. Liu, L. Zhao, L. Cao, S. Jiang and H. Hou, *Compos. Commun.*, **9**, 76 (2018).
2. L. Jiang, Y. Wang and C. Feng, *Procedia Eng.*, **45**, 993 (2012).
3. M. M. Mahlambi, A. K. Mishra, S. B. Mishra, A. M. Raichur, B. B. Mamba and R. W. Krause, *J. Nanomaterials*, 2012, Article ID 302046 (2012)
4. F. Huang, A. Yan and H. Zhao, *Semiconductor photocatalysis materials-mechanisms and applicaations*, IntechOpen Limited, London (2016).
5. H. Khojasteh, M. Salavati-Niasari and S. Mortazavi-Derazkola, *J. Mater. Sci.: Mater. Electron.*, **27**(4), 3599 (2016).
6. M. Manzoor, A. Rafiq, M. Ikram, M. Nafees and S. Ali, *Int. Nano Lett.*, **8**(1), 1 (2018).
7. R. Bashiri, M. M. Norani, C. F. Kait and S. Sufian, *Adv. Mater. Res.*, **925**, 248 (2014).
8. S. Woo, W. Kim, S. Kim and C. Rhee, *Mater. Sci. Eng.: A*, **449**, 1151 (2007).
9. G. Nakhate, V. Nikam, K. Kanade, S. Arbuj, B. Kale and J. Baeg, *Mater. Chem. Phys.*, **124**(2-3), 976 (2010).
10. S. K. Khore, S. R. Kadam, S. D. Naik, B. B. Kale and R. S. Sonawane, *New J. Chem.*, **42**(13), 10958 (2018).
11. K. Prabakar, T. Takahashi, T. Nezuka, K. Takahashi, T. Nakashima, Y. Kubota and A. Fujishima, *Renew. Energy*, **33**(2), 277 (2008).
12. K. Song, X. Han and G. Shao, *J. Alloys Compd.*, **551**, 118 (2013).
13. T. Sakthivel, K. A. Kumar, J. Senthilselvan and K. Jagannathan, *J. Mater. Sci.: Mater. Electron.*, **29**(3), 2228 (2018).
14. D. Ding, C. Ning and X. Wang, *RSC Adv.*, **5**(116), 95478 (2015).
15. B. Gao, T. Wang, X. Fan, H. Gong, H. Guo, W. Xia, Y. Feng, X. Huang and J. He, *Inorg. Chem. Front.*, **4**(5), 898 (2017).
16. S. Buddee, C. Suwanchawalit and S. Wongnawa, *Dig. J. Nanomater. Biostruct.*, **12**(3), 829 (2017).
17. T. Hirakawa and P. V. Kamat, *J. Am. Chem. Soc.*, **127**(11), 3928 (2005).
18. J. Y. Park, K. I. Choi, J. H. Lee, C. H. Hwang, D. Y. Choi and J. W. Lee, *Mater. Lett.*, **97**(15), 64 (2013).
19. B. Guan, J. Yu, S. Guo, S. Yu and S. Han, *Nanoscale Adv.*, **2**, 1352 (2020).
20. G. Nagaraj, R. Senthil, R. Boddula and K. Ravichandaran, *Curr. Anal. Chem.*, **17**, 279 (2021).
21. D. Jing, Y. Zhang and L. Guo, *Chem. Phys. Lett.*, **415**(1-3), 74 (2005).
22. T. Wang, X. Meng, G. Liu, K. Chang, P. Li, Q. Kang, L. Liu, M. Li, S. Ouyang and J. Ye, *J. Mater. Chem. A*, **3**(18), 9491 (2015).
23. R. Nirmala, H. Y. Kim, C. Yi, N. A. Barakat, R. Navamathavan and M. El-Newehy, *Int. J. Hydrogen Energy*, **37**(13), 10036 (2012).
24. H. Albetran, Y. Dong and I. M. Low, *J. Asian Ceram. Societies*, **3**(4), 292 (2015).
25. C. Wang, Y. Tong, Z. Sun, Y. Xin, E. Yan and Z. Huang, *Mater. Lett.*, **61**(29), 5125 (2007).
26. W. Sigmund, J. Yuh, H. Park, V. Maneeratana, G. Pyrgiotakis, A. Daga, J. Taylor and J. C. Nino, *J. Am. Ceram. Soc.*, **89**(2), 395 (2006).
27. J. Y. Park and S. S. Kim, *Metals Mater. Int.*, **15**(1), 95 (2009).
28. I. S. Chronakis, *J. Mater. Process. Technol.*, **167**(2-3), 283 (2005).
29. S. Aryal, C. K. Kim, K.-W. Kim, M. S. Khil and H. Y. Kim, *Mater. Sci. Eng.: C*, **28**(1), 75 (2008).
30. D. Cahyaningsih, A. Taufik and R. Saleh, *J. Phys.: Conf. Ser.*, **1442**, 012017 (2020).
31. S. Rajeh, A. Barhoumi, A. Mhamdi, G. Leroy, B. Duponchel, M. Amlouk and S. Guermazi, *Bull. Mater. Sci.*, **39**, 177 (2016).
32. Y. Nishihata, J. Mizuki, T. Akao, H. Tanaka, M. Uenishi, M. Kimura, T. Okamoto and N. Hamada, *Nature*, **418**, 164 (2002).
33. B. Ding, C. K. Kim, H. Y. Kim, M. K. Seo and S. J. Park, *Fibers Polym.*, **5**(2), 105 (2004).
34. J. Zhang, P. Zhou, J. Liu and J. Yu, *Phys. Chem. Chem. Phys.*, **16**(38), 20382 (2014).
35. D. J. Deka, J. Kim, S. Gunduz, M. Aouine, J.-M. M. Millet, A. C. Co and U. S. Ozkan, *Appl. Catal. B: Environ.*, **286**, 119917 (2021).
36. D. S. Kim, S. J. Han and S.-Y. Kwak, *J. Colloid Interface Sci.*, **316**(1), 85 (2007).
37. S. Chen, Y. Xiao, Y. Wang, Z. Hu, H. Zhao and W. Xie, *Nanomaterials*, **8**(4), 245 (2018).
38. A. Janotti, J. Varley, P. Rinke, N. Umezawa, G. Kresse and C. G. Van de Walle, *Phys. Rev. B*, **81**(8), 085212 (2010).
39. G. Wang, H. Wang, Y. Ling, Y. Tang, X. Yang, R. C. Fitzmorris, C. Wang, J. Z. Zhang and Y. Li, *Nano Lett.*, **11**(7), 3026 (2011).
40. N. Feng, F. Liu, M. Huang, A. Zheng, Q. Wang, T. Chen, G. Cao, J. Xu, J. Fan and F. Deng, *Sci. Rep.*, **6**, 1 (2016).
41. A. Lepcha, C. Maccato, A. Mettenbörger, T. Andreu, L. Mayrhofer, M. Walter, S. Olthof, T.-P. Ruoko, A. Klein and M. Moseler, *J. Phys. Chem. C*, **119**, 18835 (2015).
42. N.-W. Lee, J.-W. Jung, J.-S. Lee, H.-Y. Jang, I.-D. Kim and W.-H. Ryu, *Electrochim. Acta*, **263**, 417 (2018).
43. D. H. Kim, D.-K. Choi, S.-J. Kim and K. S. Lee, *Catal. Commun.*, **9**(5), 654 (2008).